Comparison of optical properties of bioaerosols composed of microbial spores and hyphae [Invited]

Xinyu Wang (王新宇)[1,2,3], Yihua Hu (胡以华)[1,2,3,*], Xing Yang (杨 星)[1,2,3,**], Youlin Gu (顾有林)[1,2,3], Haihao He (何海浩)[1,2,3], Wanying Ding (丁婉莹)[1,2,3], and Peng Wang (王 鹏)[4]

[1] Electronic Countermeasure Institute, National University of Defense Technology, Hefei 230037, China

[2] State Key Laboratory of Pulsed Power Laser Technology, National University of Defense Technology, Hefei 230037, China

[3] Advanced Laser Technology Laboratory of Anhui Province, Hefei 230037, China

[4] Key Laboratory of High Magnetic Field and Ion Beam Physical Biology, Hefei Institute of Physical Science, Chinese Academy of Sciences, Hefei 230037, China

*Corresponding author: skl_hyh@163.com
**Corresponding author: yangxing17@nudt.edu.cn

Bioaerosols exhibit significant broadband extinction performance and have vital impacts on climate change, optical detection, communication, disease transmission, and the development of optical attenuation materials. Microbial spores and microbial hyphae represent two primary forms of bioaerosol particles. However, a comprehensive investigation and comparison of their optical properties have not been conducted yet. In this paper, the spectra of spores and hyphae were tested, and the absorption peaks, component contents, and protein structural differences were compared. Accurate structural models were established, and the optical attenuation parameters were calculated. Aerosol chamber experiments were conducted to verify the optical attenuation performance of microbial spores and hyphae in the mid-infrared and far-infrared spectral bands. Results demonstrate that selecting spores and hyphae can significantly reduce the average transmittance from 21.2% to 6.4% in the mid-infrared band and from 31.3% to 19.6% in the far-infrared band within three minutes. The conclusions have significant implications for the selection of high-performance microbial optical attenuation materials as well as for the rapid detection of bioaerosol types in research on climate change and the spread of pathogenic aerosols.

Keywords: bioaerosol; optical properties; optical materials; light-matter interactions; Fourier transform infrared spectra.
DOI: 10.3788/COL202321.090006

1. Introduction

Bioaerosol is an important component of the atmosphere. First, bioaerosols may affect the amount of solar radiation reaching the surface by scattering and absorption, which regulates the radiation budget of the Earth-atmosphere system and influences climate change[1,2]. Therefore, studying the optical properties of bioaerosols is of great significance for climate change research[3]. Second, as a potential optical attenuation material, research on the optical properties of biological aerosols is conducive to their better utilization. For example, bioaerosols can be released in a certain area to attenuate solar radiation and to alleviate greenhouse effect or to attenuate optical signals or electromagnetic radiation in industry, aerospace, and military fields. In addition, the quantification of aerosol size through optical trapping is also an important optical application for bioaerosols, which involves trapping and manipulating single airborne particles by optical configurations[4,5]. Finally, the spatial and temporal distributions and transport characteristics of atmospheric bioaerosols

will cause environmental pollution and even disease transmission[6,7]. Bioaerosol species can be rapidly detected and identified[8,9] by their optical properties for further disease prevention and control.

Various microorganisms are the main components of atmospheric bioaerosols, and their main forms are divided into microbial spores and microbial hyphae. Previous research has demonstrated the broadband optical attenuation performance of various pollen, yeast, and microbial spores[10]. The complex refractive index of microbial materials has been calculated[11]. The difference of infrared attenuation performance between bioaerosols and traditional smoke materials has been compared[12], and the influence of relative humidity on the broadband attenuation performance of bioaerosols was studied[13]. However, a comparative analysis on the optical properties of bioaerosols composed of microbial spores and hyphae is lacking. This research is extremely necessary. On the one hand, as two main forms of microorganisms, comparing the optical

properties of bioaerosols composed of microbial spores and hyphae in different wavebands can better select bioaerosols with good optical performance for application in climate change, industry, aerospace, and military fields. On the other hand, for pathogenic microbial aerosols, the pathogenicity of bioaerosols composed of microbial spores is stronger than those composed of homogenous microbial hyphae. Rapid detection of the optical properties of bioaerosols can distinguish pathogenic microbial spores and hyphae in the atmosphere, assisting in further targeted aerosol transmission interruption and prevention and control of infectious diseases.

The composition particles of bioaerosols are often various particles released from terrestrial and marine ecosystems into the atmosphere. They are composed of biological and non-biological components, including organisms such as fungi, bacteria, viruses, and pollen and their excretions. This article focuses on artificially prepared bioaerosols used for optical attenuation. The advantages of this type of aerosol are wideband strong attenuation achieved by a single material, long floating time, and safety. Herein, we established corresponding structural models after observing the morphology of homogeneous microbial spores and hyphae, respectively. By testing the Fourier transform infrared (FT-IR) spectra of microbial spores and hyphae, the differences of their functional groups and infrared absorption peaks were determined. The differences in optical properties were further analyzed by fitting the contents of macromolecular components and secondary structure contents of proteins in homogeneous microbial spores and hyphae. Based on the established structural models, the discrete dipole approximation (DDA) method was used to calculate the optical attenuation coefficients of microbial spores and hyphae in the band of 2.5–14.5 μm. The Monte Carlo algorithm was used to calculate the transmittance of the bioaerosols composed of microbial spores and hyphae. Finally, the optical properties of bioaerosols composed of microbial spores and hyphae were tested through aerosol chamber experiment, and the reliability of the simulation results was proved.

2. Material and Methods

2.1. Materials preparation

Aspergillus niger spores are a common type of microbial spores that have been shown to exhibit significant broadband optical properties[10,12,13]. Therefore, they are suitable research objects for this study. AN0408 is a strain of *Aspergillus niger*. The specific preparation process of AN0408 spores and hyphae can be divided into five steps: strains activation → seed liquid culture → fermentation in a fermenter → stains collection → sample drying. Among them, the main differences in the cultivation process for AN0408 spores and AN0408 hyphae lied in the fermentation and collection processes: solid fermentation was used for the culture of the AN0408 spores, while liquid fermentation was used for the AN0408 hyphae. In addition, centrifugal precipitation was used for the collection of the

AN0408 spores, while layered filtration was used for the AN0408 hyphae. For further comparative analysis, the AN0408 spores and hyphae were inactivated by a damp-heat inactivation method (inactivation temperature 121℃, inactivation time 30 min). In this way, the inactivated AN0408 spores and hyphae were obtained.

Scanning electron microscopy (SEM) images of AN0408 spores and hyphae before and after inactivation are shown in Fig. 1. As shown in the figure, the morphology of the AN0408 spores was an oblate cylinder with slightly concave ends and a number of folds and protrusions on the surface. The overall shape resembled a pumpkin. The morphology of AN0408 spores showed less variation after inactivation. The radius of a single spore was approximately 2.5 μm. The morphology of the AN0408 hyphae was an irregular block with slightly irregular folds on the surface. Compared with the inactivated hyphae, the morphology of the AN0408 hyphae is larger and flatter, while the AN0408 mycelia become smaller and slender after inactivation. According to the morphological characteristics shown in the SEM images of the AN0408 spores and hyphae before and after inactivation, corresponding structural models were established for subsequent calculations of optical attenuation coefficients. Different from commonly used regular particle shapes such as spheres, ellipsoids, cylinders, and chains in previous research, this study has developed structural models that offer more intricate details and closely resemble the actual shapes of biological aerosol particles observed in the SEM images. For instance, the spore model consists of a slightly concave circular disc with added random noise to mimic the wrinkled surface of irregularly shaped particles. Various typical structures observed in the SEM images for microbial spores have been utilized to generate corresponding structure models. These structure models were constructed using Blender, and 3D structure
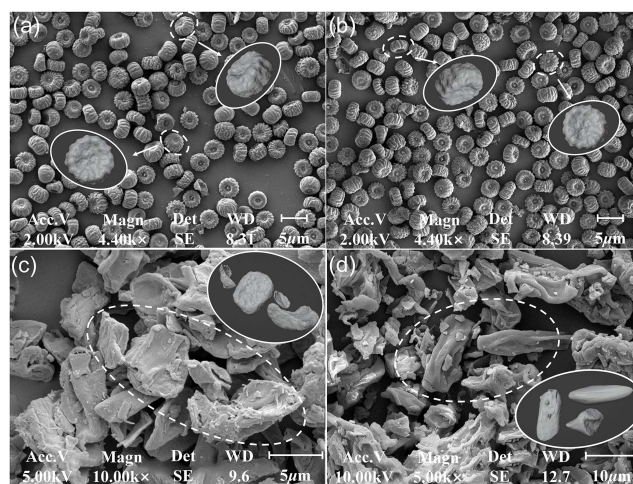

Fig. 1. SEM images of AN0408 spores and hyphae. The actual structures of the AN0408 spores and hyphae are shown in the white dashed boxes in the figure, and their corresponding structural models are encircled in white solid line ellipses in the same subgraph. (a) AN0408 spores, (b) inactivated AN0408 spores, (c) AN0408 hyphae, and (d) inactivated AN0408 hyphae.

data has been exported for subsequent simulation analysis. The actual structures of the AN0408 spores and hyphae were shown in the white dashed boxes in the figure, and their corresponding structural models were encircled in a white solid line in the same subgraph.

2.2. FT-IR spectrum measurement and complex refractive index calculation

FT-IR spectroscopy[14–16] has been widely used for the molecular identification and structural characterization of protein secondary mechanisms. FT-IR spectroscopy is a powerful tool for examining biological molecules because the characteristics of functional groups can be determined by IR absorption[17]. The IR spectra exhibit unique molecular vibrational modes for each functional group. The composition and structures of functional groups can be determined from the position, width, and intensity of the spectra[18].

The FT-IR spectra of AN0408 spores and hyphae samples were measured in the range of 400–4000 cm^{-1} using a Fourier transform infrared spectroscope (Nicolet iS50, Thermo Fisher Scientific, USA) equipped with an attenuated total reflection (ATR) accessory. Each spectrum of the reflection mode was obtained using an average of 32 consecutive scans with a resolution of 0.482 cm^{-1} and scanning interval of 0.482 cm^{-1}. Each sample was measured three times, and the average spectra were calculated.

Using the measured FT-IR spectra, the complex refractive index (CRI) of the AN0408 spores and hyphae in the 2.5–14.5 μm waveband was calculated using the Kramers–Kronig (K-K) algorithm[11],

$$\Theta(\lambda) = \frac{\lambda}{\pi} P \int_0^\infty \frac{\ln R(\lambda')}{\lambda'^2 \lambda^2} d\lambda', \qquad (1)$$

where $R(\lambda)$ is the vertical reflectivity, P is the Cauchy principal value function, and λ is the wavelength. The real parts (n) and imaginary parts (k) of the complex refractive index (m) can be obtained as

$$n(\lambda) = \frac{1 - R(\lambda)}{1 + R(\lambda) + 2\sqrt{R(\lambda)} \cos \Theta(\lambda)}, \qquad (2)$$

$$k(\lambda) = \frac{-2\sqrt{R(\lambda)} \cos \Theta(\lambda)}{1 + R(\lambda) + 2\sqrt{R(\lambda)} \cos \Theta(\lambda)}, \qquad (3)$$

$$m(\lambda) = n(\lambda) + k(\lambda). \qquad (4)$$

It is known that the $R(\lambda)$ should be obtained in the full band to calculate the complex refractive index. However, in the actual experimental measurements, the $R(\lambda)$ has been measured only in the limited band (2.5 to 14.59 μm). The constant extrapolation method was used to expand the range of reflectivity. A value of 100 μm was used as the upper limit of the integral because the reflectivity above 100 μm had little effect on the complex

refractive index in the 2.5 to 14.59 μm wavelength range. $R(0–2.5\,\mu m) = R(2.5\,\mu m)$, and $R(14.59–100\,\mu m) = R(14.59\,\mu m)$. Therefore, $R(\lambda)$ over the entire integral range (0–100 μm) was acquired.

2.3. Optical attenuation coefficient calculation and transmittance simulation

The DDA method is an approximation method that is used to solve the volume integral equation of electromagnetic scattering. It is an important method used to study the scattering characteristics of particles[19–21]. As long as the CRI, denoted as m, satisfies the condition $|m - 1| \leq 3$, the DDA method is applicable to scatterers of any geometric shape, and the scatterers can be anisotropic and non-uniform[22].

Using this method, the extinction cross section C_{ext}, the scattering cross section C_{sca}, and the absorption cross section C_{abs} of the AN0408 spores and hyphae can be calculated[23–25].

In addition, the densities ρ of the AN0408 spores and hyphae in corresponding bioaerosols and the optical length L were set to suitable parameter values, respectively. All particles were assumed to be evenly distributed in space. With these parameters, the transmittance of incident light through the AN0408 bioaerosols can be simulated using the Monte Carlo algorithm[26].

2.4. Transmittance experiment in an aerosol chamber

In this experiment, we focused on the transmittance of bioaerosols produced by the AN0408 spores and hyphae in the mid-infrared (MIR) band and far-infrared (FIR) band. As shown in Fig. 2, we designed an aerosol chamber (4 m × 3 m × 2.4 m) to perform the transmittance experiment. Two pairs of light sources and detectors were placed on both sides of the chamber to measure the transmittance in the MIR and FIR bands. The light sources are black bodies (HFX-300A, Fuyuan, China), for which the temperature can be set to 5°C–400°C. The detectors for the MIR and FIR bands are the MIR thermal imager (SC7700M, FLIR, USA) and the FIR thermal imager (VarioCAM HD, InfraTec, Germany), respectively. The optical
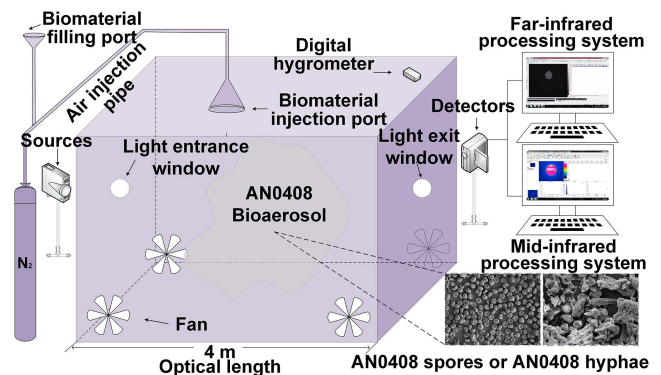

Fig. 2. Schematic of the broadband transmittance experiment in the bioaerosol chamber.

length between each pair of light sources and detectors was 4 m. Then, 40 mg of biomaterials was weighed and filled into the filling port of the aerosol chamber. The materials were injected into the aerosol chamber using N_2 gas (output pressure of 0.5 MPa). Fans were placed at the four corners of the aerosol chamber to accelerate the dispersion of the biomaterials and better disperse the materials in the confined space of the aerosol chamber. As the spores were evenly distributed in the aerosol chamber, the average power of the light signal received by the detector over 3 min was recorded. Using these data, the transmittance could be calculated. A high-precision temperature and humidity recorder (174H, Testo, Germany) was used to record real-time changes of the temperature and relative humidity inside the aerosol chamber.

3. Results and Discussion

The ATR FT-IR spectra of the AN0408 spores and hyphae are shown in Fig. 3(a). As shown in the figure, both spores and hyphae exhibit similar trends in reflectance. As for the changes before and after inactivation, the changes of hyphae were not obvious. However, the reflectance intensities of the spores varied greatly. The results of the characteristic peaks identification are presented in Fig. 3(b), where the vertical axis of the original spectra was converted from reflectance to absorbance. As shown in Fig. 3(b), the characteristic peaks of the AN0408 spores and hyphae were similar, which indicated that the types of absorptive functional groups contained in the spores and the hyphae showed little difference. However, there are slight differences in the positions of the absorption peaks, and the relative intensities of the absorption peaks differ noticeably. This suggests that although the composition of spores and hyphae of the same microbial strain is similar, there are differences in the content of each component.

Compared to spores, hyphae showed a significant decrease in the C=O and N–H peaks around $1652\,\mathrm{cm}^{-1}$ and $1544\,\mathrm{cm}^{-1}$, and a significant increase in the polysaccharide C−O absorption peaks at $1076\,\mathrm{cm}^{-1}$ and $1039\,\mathrm{cm}^{-1}$. This result indicates that spores accumulate more polysaccharide structures and have reduced content of structural proteins after developing into hyphae. Compared to inactivated spores, inactivated hyphae exhibited a shoulder peak trend in the $3100–3300\,\mathrm{cm}^{-1}$ region,
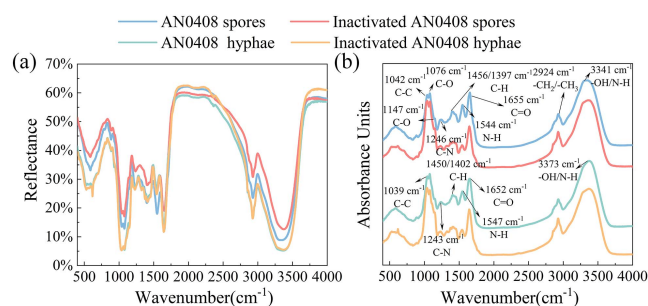
Table 1. Relative Contents of Proteins, Polysaccharides, and Fatty Acids.

Sample	Content		
	Protein	Polysaccharide	Aliphatic acid
AN0408 spores	5.65%	9.65%	4.11%
AN0408 hyphae inactivated	4.7%	14.37%	4.66%
AN0408 spores inactivated	4.22%	9.68%	7.28%
AN0408 hyphae	5.11%	13.84%	4.41%

indicating a difference in the content of triterpenes and sterols between the two samples. Additionally, a significant decrease is observed in the N–H absorption peak of the amide band at $1547\,\mathrm{cm}^{-1}$, confirming differences in the main chemical components (proteins, fatty acids, etc.) between inactivated spores and hyphae.

To analyze these differences more effectively, the FT-IR spectra were subjected to peak fitting using the GaussAmp function in Peakfit v4.21. This work was done to determine the differences in relative intensities of major components (proteins, polysaccharides, fatty acids, etc.) in the AN0408 spores and hyphae. The fitting method employed is as follows: the relative intensities of peaks in the range of $2800–2950\,\mathrm{cm}^{-1}$ were summed to represent the fatty acid compounds, the relative intensity of the amide I band (around $1650\,\mathrm{cm}^{-1}$) was used to represent the protein substances, and the relative intensities of peaks in the range of $1000–1150\,\mathrm{cm}^{-1}$ were summed to represent the polysaccharide compounds, reflecting changes in their content. The relative content of protein, polysaccharide, and fatty acid compounds in the AN0408 spores and hyphae before and after inactivation, obtained through the fitting process, is presented in Table 1. Additionally, a secondary structural fitting of the amide I band was performed to analyze protein conformation, and the results are shown in Fig. 4.

The fitting results indicate that compared to inactivated spores, the relative content of the polysaccharides in the inactivated hyphae significantly increased from 9.68% to 13.84%. The relative content of proteins showed a slight increase, while the relative content of aliphatic acids decreased by about 3%. This could be attributed to the less active metabolism of the spores, resulting in lower requirements for enzymes and protein functions, thus leading to lower protein expression in the spores. The fitting results of the amide I band showed a slight decrease in the relative intensity of the random coil structures in the inactivated hyphae, indicating a difference in protein specificity between inactivated spores and hyphae, with slightly higher protein activity in the hyphae. Morphological changes, nutrient requirements, cell osmotic pressure maintenance, and changes in internal and external environments during different stages may be the main factors contributing to the differences in polysaccharide and fatty acid content between the spores and the hyphae. The relative intensity changes of the protein secondary
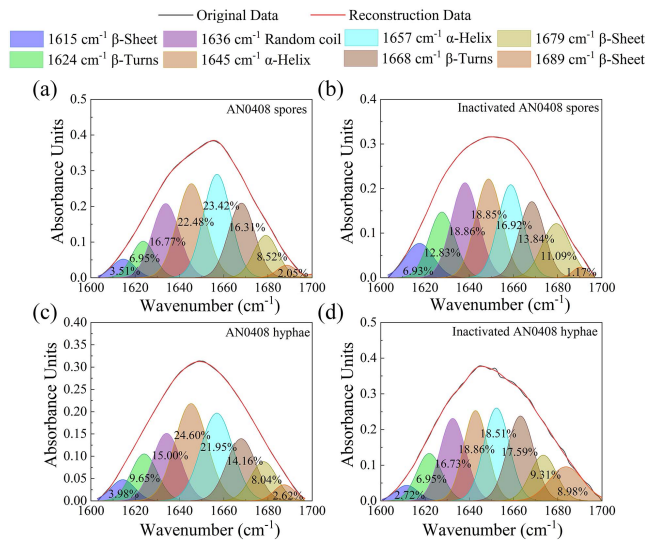

Fig. 3. (a) ATR FT-IR spectra and (b) characteristic peaks of AN0408 spores and hyphae for ATR FT-IR spectra.

Fig. 4. Protein secondary structure fitting results.

Fig. 6. Results of the DDA method and the Monte Carlo algorithm.

structures of the spores and the hyphae followed a similar pattern: compared to spores, the relative intensity of random coil structures in hyphae slightly decreased, and the relative content of fatty compounds increased by about 0.5%, indicating slightly higher protein activity in the hyphae.

As shown in Fig. 5, the real part n of CRI of the four samples ranged from 1.1 to 1.8. The n of the inactivated spores, the inactivated hyphae, and the hyphae and spores increase in turn and the differences are obvious. The imaginary part k of the spores and the hyphae showed significant differences in the relative magnitude at different wavelengths, indicating significant differences in the absorption capabilities of spores and hyphae in various wavebands. Each sample has advantageous wavebands with high absorption coefficients.

The results of the optical attenuation coefficients for the four samples are shown in Figs. 6(a)–6(c). The extinction cross section, absorption cross section, and scattering cross section of the inactivated hyphae were greater than the corresponding parameters of inactivated spores in the 2.5–14.5 μm waveband. The scattering ability of the spores in the 4–6 μm waveband was superior to that of hyphae, which may be due to the fact that the average radius of the spores is around 2.5 μm, which is close to the wavelength of the incident light. However, due to
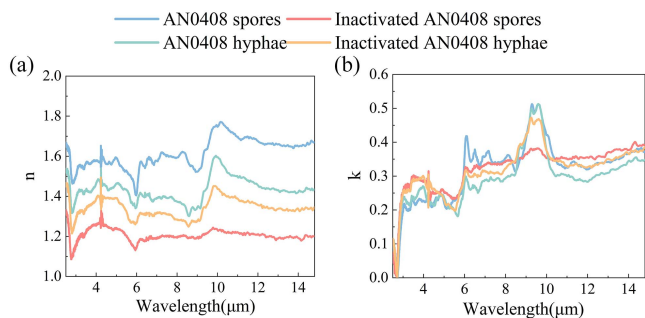

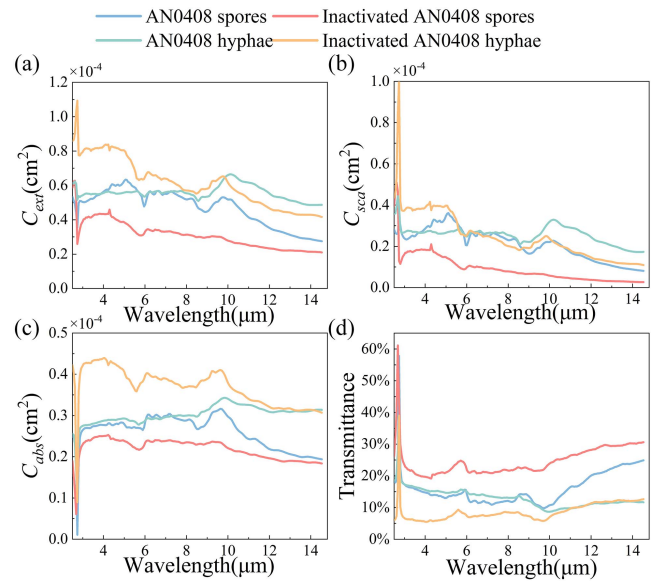**Fig. 5.** CRI of active and inactivated spores and hyphae.

differences in composition, the optical absorption ability of the hyphae is stronger in the 2.5–6 μm waveband. In the 8.4–14.5 μm waveband, due to the larger particle size of the hyphae and its closer proximity to the wavelength of the incident light, its optical attenuation ability is significantly superior to that of the spores. The transmittance results obtained through the Monte Carlo algorithm are shown in Fig. 6(d). As shown in the figure, all four spores and hyphae samples can attenuate the transmittance of incident light in the 2.5–14.5 μm waveband to below 30%. Among them, inactivated hyphae exhibited the strongest attenuation ability, reducing the transmittance to 5%–10%, while inactivated spores showed the weakest attenuation ability, maintaining the transmittance at 20%–30%.

The transmittance of the AN0408 spores and hyphae before and after inactivation was tested using an aerosol chamber. In this experiment, the transmittance of each type of bioaerosols was tested three times, and the average of the three tests was recorded. Each test lasted for 3 min, starting when the biological materials were sprayed into the aerosol chamber. The mass of the biological materials sprayed in each test was 40 g. The average transmittance of the four bioaerosols in the MIR and FIR bands is shown in Fig. 7. The negative time values in the figure represent the period before the biological materials were sprayed, during which the transmittance was 100%.

As shown in Fig. 7, all four bioaerosols exhibit significant attenuation performance in both the MIR and FIR bands. The optical attenuation ability of the AN0408 spores in the MIR band is stronger than that of the AN0408 hyphae. AN0408 spores can reduce the transmittance to below 12% within 3 min, while the AN0408 hyphae can maintain the transmittance below 18% within 3 min. Conversely, the AN0408 hyphae have a stronger attenuation capability in the FIR band, reducing the transmittance to 20%–25% within 3 min, while the AN0408 spores can only maintain the transmittance of 20%–35%. Inactivated AN0408 hyphae have better attenuation capabilities
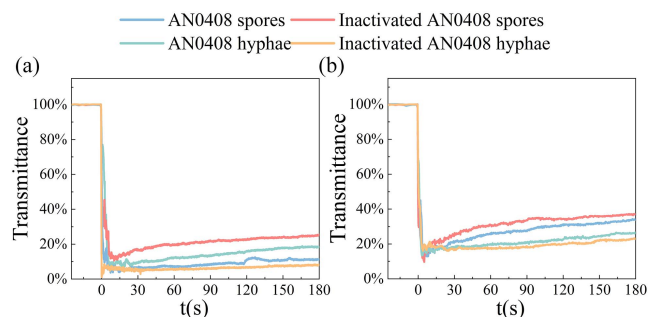
Fig. 7. Results of the aerosol chamber test for (a) the MIR band and (b) the FIR band.
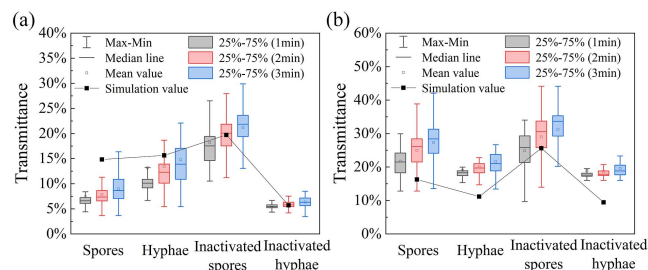

Fig. 8. Comparison of experimental results with simulation results for (a) the MIR band and (b) the FIR band.

in both bands compared to the inactivated AN0408 spores. Inactivated hyphae can reduce the transmittance in the MIR band to 5%–8% and in the FIR band to around 20%. Inactivated spores can reduce the transmittance in the MIR band to 12%–25% and in the FIR band to below 35% within 3 min.

To compare the simulation results with the aerosol chamber test results, the average transmittance simulation results of the four aerosols in the corresponding bands are plotted in Fig. 8. The test results of the transmittance in the aerosol chamber in 1 min, 2 min, and 3 min are shown in the box plots in Fig. 8. As shown in Fig. 8, the optical attenuation performance of the spores and the hyphae in different bands obtained from the aerosol chamber experiments follows the same pattern as the Monte Carlo simulation results. However, there are slight differences in the numerical values. This is because the simulation assumes that all bioaerosol particles are uniformly distributed, and their concentration is constant. In the experiment, there may be uneven distribution of aerosol particles, and the settling of particles can further affect the particle concentration in the aerosol chamber. These factors contribute to the numerical discrepancies between the experimental and simulated results.

4. Conclusion

There are significant differences in particle morphology between spores and hyphae of the same microbial strain. During the germination of spores into hyphae, it shows significant changes in

the contents of various components as well as in the activity and structural stability of the proteins. These structural differences and compositional changes result in significant discrepancies in the optical properties of bioaerosols composed of spores and hyphae.

The results of the DDA method show that the inactivated AN0408 hyphae have the largest extinction cross section, with a range of 0.5–0.8, and the inactivated AN0408 spores have the smallest extinction cross section, with a range of 0.25–0.4. Due to particle size, the extinction cross section of the AN0408 spores in the 4–6 μm band is greater than that of AN0408 hyphae, while in the 6–14.5 μm band, the extinction cross section of the AN0408 hyphae is greater.

The results of Monte Carlo simulations and aerosol chamber experiments both indicated that both the AN0408 spores and hyphae, before and after inactivation, exhibit significant optical attenuation abilities in the MIR and FIR bands. In the MIR band, the order of optical attenuation performance from the strongest to the weakest is inactivated AN0408 hyphae, AN0408 spores, AN0408 hyphae, and inactivated AN0408 spores. In the FIR band, the attenuation performance of the AN0408 hyphae is superior to that of the AN0408 spores. In practical applications, by selecting preferred spores or hyphae, the resulting bioaerosol can reduce the average transmittance in the MIR band from 21.2% to 6.4% within 3 min and reduce the average transmittance in the FIR band from 31.3% to 19.6%.

The conclusions have significant implications for future research. First, the differences in optical properties between spores and hyphae can be used for rapid discrimination of bioaerosol types in atmospheric detection, contributing to the study of climate change, environmental pollution, and disease transmission. Second, as a highly potential optical attenuation material, the differences in optical properties between bioaerosols composed of spores and hyphae can be used to select optical attenuation materials for specific target wavebands, which can significantly reduce the transmittance. Third, the established spores and hyphae structural models are more consistent with the actual structural characteristics of the particles, which can enhance the accuracy of the optical performance calculations.

References

1. R. J. Charlson, S. E. Schwartz, J. M. Hales, R. D. Cess, J. A. Coakley, J. E. Hansen, and D. J. Hofmann, "Climate forcing by anthropogenic aerosols," Science **255**, 423 (1992).
2. Y. Zhao, J. Ding, Y. Han, T. Lu, Y. Zhang, and H. Luo, "Aerosol physical–optical properties under different stages of continuous wet weather over the Guangdong–Hong Kong–Macao Greater Bay Area, China," Remote Sens. **15**, 1413 (2023).
3. J. Fröhlich-Nowoisky, C. J. Kampf, B. Weber, J. A. Huffman, C. Pöhlker, M. O. Andreae, N. Lang-Yona, S. M. Burrows, S. S. Gunthe, W. Elbert, H. Su, P. Hoor, E. Thines, T. Hoffmann, V. R. Després, and U. Pöschl, "Bioaerosols in the Earth system: climate, health, and ecosystem interactions," Atmos. Res. **182**, 346 (2016).
4. Z. Gong, Y.-L. Pan, G. Videen, and C. Wang, "Optical trapping and manipulation of single particles in air: principles, technical details, and applications," J. Quant. Spectrosc. Radiat. Transf. **214**, 94 (2018).

5. L. Zhang, A. Szmalenberg, K. Cook, B. Liu, L. Ding, F. Wang, and D. McGloin, "Trapped aerosol sizes under fiber-based counterpropagation optical trapping," J. Opt. Soc. Am. B **40**, 460 (2023).

6. B. D. Erath and A. R. Ferro, "Infectious disease transmission from bioaerosols," J. Expo. Sci. Environ. Epidemiol. **32**, 645 (2022).

7. D. Tang, T. Wei, J. Yuan, H. Xia, and X. Dou, "The transport of bioaerosols observed by wideband integrated bioaerosol sensor and coherent Doppler lidar," Atmos. Meas. Tech. **15**, 2819 (2022).

8. M. Kaliszewski, E. A. Trafny, M. R. Włodarski, R. Lewandowski, M. Stępińska, M. Kwaśny, J. Kostecki, and K. Kopczyński, "Real-time analysis and classification of bioaerosols based on optical scattering properties," Biuletyn Wojskowej Akademii Technicznej **66**, 27 (2017) https://doaj.org/article/57fff247e9234605933b135ee243889c.

9. M. Hernandez, A. E. Perring, K. McCabe, G. Kok, G. Granger, and D. Baumgardner, "Chamber catalogues of optical and fluorescent signatures distinguish bioaerosol classes," Atmos. Meas. Tech. **9**, 3283 (2016).

10. Y. Hu, X. Zhao, Y. Gu, X. Chen, X. Wang, P. Wang, Z. Zheng, and X. Dong, "Significant broadband extinction abilities of bioaerosols," Sci. China Mater. **62**, 1033 (2019).

11. Y. Gu, Y. Hu, X. Zhao, and X. Chen, "Determination of infrared complex refractive index of microbial materials," J. Quant. Spectrosc. Radiat. Transf. **217**, 305 (2018).

12. X. Zhao, Y. Hu, Y. Gu, X. Chen, X. Wang, P. Wang, and X. Dong, "A comparison of infrared extinction performances of bioaerosols and traditional smoke materials," Optik **181**, 293 (2019).

13. X. Wang, Y. Hu, Y. Gu, X. Zhao, and X. Chen, "Effects of relative humidity on the broadband extinction performance of bioaerosol," Opt. Express **27**, 23801 (2019).

14. M. C. S. Ribeiro, G. S. Senesi, J. S. Cabral, C. Cena, B. S. Marangoni, C. Kiefer, and G. Nicolodelli, "Evaluation of rice varieties using LIBS and FTIR techniques associated with PCA and machine learning algorithms," Appl. Opt. **59**, 10043 (2020).

15. A. El-Hussein, I. Yousef, and M. A. Kasem, "Exploiting FTIR microspectroscopy and chemometric analysis in the discrimination between Egyptian ancient bones: a case study," J. Opt. Soc. Am. B **37**, A110 (2020).

16. N. Li, Y. Wang, and K. Xu, "Fast discrimination of traditional Chinese medicine according to geographical origins with FTIR spectroscopy and advanced pattern recognition techniques," Opt. Express **14**, 7630 (2006).

17. R. Gurbanov, N. S. Ozek, S. Tunçer, F. Severcan, and A. G. Gozen, "Aspects of silver tolerance in bacteria: infrared spectral changes and epigenetic clues," J. Biophotonics **11**, e201700252 (2018).

18. R. Gurbanov, S. Tunçer, S. Mingu, F. Severcan, and A. G. Gozen, "Methylation, sugar puckering and Z-form status of DNA from a heavy metal-acclimated freshwater *Gordonia* sp," J. Photochem. Photobiol. B Biol. **198**, 111580 (2019).

19. I. Moradi, P. Stegmann, B. Johnson, V. Barlakas, P. Eriksson, A. Geer, R. Gelaro, S. Kalluri, D. Kleist, Q. Liu, and W. Mccarty, "Implementation of a discrete dipole approximation scattering database into community radiative transfer model," J. Geophys. Res. Atmos. **127**, e2022JD036957 (2022).

20. Y. Yang, N. Ma, J. Duan, J. Qi, Y. Zhao, Y. Wang, Y. Han, Z. Huang, and T. Lu, "Light scattering by pores in YAG transparent ceramics simulated by DDA model," J. Am. Ceram. Soc. **104**, 256 (2021).

21. N. Nees, L. Pflug, B. Mann, and M. Stingl, "Multi-material design optimization of optical properties of particulate products by discrete dipole approximation and sequential global programming," Struct. Multidiscip. Optim. **66**, 5 (2023).

22. B. T. Draine and P. J. Flatau, "User guide for the discrete dipole approximation code DDSCAT 7.3," arXiv:1305.6497 (2013).

23. T. Kozasa, J. Blum, and T. Mukai, "Optical properties of dust aggregates: II. Angular dependence of scattered light," Astron. Astrophys. **276**, 278 (1993).

24. M. Lattuada, W. Hua, and M. Morbidelli, "Radial density distribution of fractal clusters," Chem. Eng. Sci. **59**, 4401 (2004).

25. M. Min, C. Dominik, J. W. Hovenier, A. de Koter, and L. B. F. M. Waters, "The 10 μm amorphous silicate feature of fractal aggregates and compact particles with complex shapes," Astron. Astrophys. **445**, 1005 (2005).

26. S. L. Jacques, "Modeling tissue optics using Monte Carlo modeling: a tutorial," Proc. SPIE **6854**, 68540T (2008).